ISSN 1560-8034, 1605-6582 (On-line), SPQEO, 2019. V. 22, N 1. P. 119-129.

Sensors

The effect of ion implantation on structural damage in compositionally graded AlGaN layers

O.I. Liubchenko[1,*], V.P. Kladko[1], H.V. Stanchu[1,2], T.M. Sabov[1], V.P. Melnik[1], S.B. Kryvyi[1,3] and A.E. Belyaev[1]

[1]*V. Lashkaryov Institute of Semiconductor Physics, National Academy of Sciences of Ukraine, 41, prosp. Nauky, 03680 Kyiv, Ukraine*
[2]*Institute for Nanoscience & Engineering, University of Arkansas, W. Dickson 731, Fayetteville, Arkansas 72701, United States*
[3]*Institute of Physics, Polish Academy of Sciences, Al. Lotników 32/46 PL-02-668 Warsaw, Poland*
[*]*E-mail: lubchenco.a@gmail.com*

Abstract. Compositionally graded $Al_xGa_{1-x}N$ alloys with the Al concentration in the ($7 \le x \le 32$) range were implanted with Ar^+ ions to study the structural and strain changes (strain engineering). It was shown that ion implantation leads to ~0.3…0.46% hydrostatic strains and a relatively low damage of the crystal structure. The ion-implantation leads mainly to an increase of the density of point defects, while the dislocation configuration is almost unaffected. The density of microdefects is sufficiently reduced after the post-implantation annealing. The structural quality of the $Al_xGa_{1-x}N$ layers strongly depends on the Al concentration and is worsen with increasing Al. The implantation induced structural changes in highly dislocated $Al_xGa_{1-x}N$ layers are generally less pronounced. Based on the X-ray diffraction, a model is developed to explain the strain field behavior in the $Al_xGa_{1-x}N$/GaN heterostructures by migration of point defects and strain field redistribution. The approach to simulate 2θ/ω scans using statistical dynamical theory of X-ray diffraction for implanted compositionally graded structures AlGaN has been developed.

Keywords: $Al_xGa_{1-x}N$, graded layers, ion implantation, statistical X-ray diffraction theory, microdefects.

doi: https://doi.org/10.15407/spqeo22.01.119
PACS 61.05.-a, 61.05.C-, 61.10.Nz, 61.72.-y, 68.55.Ln, 68.65.-k, 78.55.Cr, 78.70.Ck

Manuscript received 07.03.19; revised version received 21.03.19; accepted for publication 27.03.19; published online 30.03.19.

1. Introduction

The wide range of direct band gaps of AlGaN alloys (from 3.4 to 6.2 eV) and the presence of strong electronic polarization fields [1] are attractive properties for the development of various optoelectronic devices. In particular, the recently demonstrated polarization-induced doping in III-nitrides was shown to effectively enhance the *p*-type conductivity of the AlGaN layers [2], which was successfully exploited for fabrication of light emitting diodes (LEDs) [2] and *p-n* junction devices [3]. At the same time, the ion implantation technique is more attractive for selective area doping and implant isolation [4].

It is well known that the implantation process leads to severe deterioration of the crystalline quality and accumulation of large lattice strains. These effects were extensively studied in the past for AlN and GaN semiconductors [5, 6], and it was shown that damage and strain buildup with increasing the ion dose until amorphization. The implantation damage is partially reduced after the post implantation high-temperature annealing, which is performed for donor/acceptor activation.

The recent studies on the process of ion implantation in ternary $Al_{0.44}Ga_{0.56}N$ layers have shown a multi-step damage accumulation with increasing the implantation fluence, and the transition threshold of the defects buildup increasing with AlN molar fraction [7]. No amorphization was reported for the AlGaN alloys implanted with Ar^+ ions at 320 keV. The accumulation of implantation damage in $Al_xGa_{1-x}N$ alloys was also investigated in Ref. [8] for $Al_{0.15}Ga_{0.85}N$ and $Al_{0.77}Ga_{0.23}N$ layers implanted under random and channeled geometries with Tm^+ ions. The damage level was shown to be lower for channeling implantation, and like in Ref. [7] the damage behavior was distinct for the alloys with different AlN molar fractions. Specifically, it

was shown that surface regions with lower damage levels form for AlGaN layers with higher AlN molar fractions. Similar behavior of the bimodal damage was also demonstrated in Ref. [9] for $Al_xGa_{1-x}N$ alloys (x = 0, 0.13, 0.47, 0.7, and 1) implanted with Ar^+ ions. In addition, the X-ray diffraction (XRD) analysis has shown that the implantation with Ar^+ ions introduces hydrostatic strain resulting from the expansion of the *c*-lattice parameter. Saturation of the strain was suggested to occur in alloys implanted at high ion fluences.

In this work, a detailed XRD study of the effect of ion implantation and post implantation annealing on the structural damage and strain state is presented for compositionally graded $Al_xGa_{1-x}N$ layers. The implications of the described results are important for further understanding of the processes of implantation damage in III-nitride alloys with compositional gradients.

2. Experiment

The $Al_xGa_{1-x}N$ layers were grown in a Veeco Gen-II plasma-assisted molecular beam epitaxy (PAMBE) system on commercial substrates consisting of ~5 μm of (0001) oriented GaN on AlN/sapphire. First, the 400-nm thick GaN buffer layer was grown under gallium-rich conditions at a substrate temperature of 690 °C. Next, the substrate temperature was raised up to 710 °C, and compositionally graded $Al_xGa_{1-x}N$ layers were grown by linearly changing the temperature of the Al effusion cell [10]. The AlN molar fraction in the $Al_xGa_{1-x}N$ layers was graded from ~7 up to ~22% (sample S1) and from ~7 up to ~32% (sample S2). Implantation was performed at room temperature at the angle 7°. Both samples were implanted with Ar^+ ions in two steps. For each step, the implantation energy and dose were 100 keV and 1×10^{14} at./cm^{-2}, respectively. The high-temperature annealing was performed at ~750 °C for 15 min. The samples were investigated with high-resolution X-ray diffraction (HRXRD) using PANalytical X'Pert Pro MRD XL diffractometer equipped with the $CuK_{\alpha1}$ radiation (λ = 0.154056 nm), four-bounce (220) Ge monochromator, and three-fold (022) Ge analyzer.

3. Theory

To simulate X-ray diffraction spectra, we use the statistical dynamical theory of X-ray diffraction developed in Refs. [11–13] for uniform epitaxial films with randomly distributed microdefects. The coherent part of the diffracted intensity from a uniform crystalline layer is based on solution of the equations for the coherent and diffuse waves [11] under the condition $\langle u\rangle = 0$ (where $\langle u\rangle$ is the statistical average of the displacement of the atoms from their positions in a perfect lattice [11, 13, 14]).

In the case of symmetric Bragg diffraction, the diffracted (E_g^c) and transmitted amplitudes (E_0^c) of X-ray waves from a plane-parallel plate of thickness *l* are given as [11]:

$$E_0^c(z) = \left(\xi_1 \exp\left[i\xi(l-z)\right] - \xi_2\right)\exp\left(i\varepsilon_1 z\right)/Q\,, \tag{1}$$

$$E_g^c(z) = E\sigma_g\left(\exp\left[i\xi(l-z)\right] - 1\right)\exp\left(i\varepsilon_1 z\right)/Q\,, \tag{2}$$

where *z* is the depth coordinate.

The amplitude coefficients of the reflected *r* and transmitted *t* waves through a layer of the thickness *l* are [11]:

$$r^{\pm g} = E\sigma_{\pm g}\left(\exp\left(il\xi\right) - 1\right)/Q\,, \tag{3}$$

$$t = \xi\exp\left(i\varepsilon_1 l\right)/Q\,, \tag{4}$$

$$t^{-g} = \xi\exp\left(-i\varepsilon_2 l\right)/Q\,, \tag{5}$$

where, [11], $Q = \xi_1\exp\left(il\xi\right) - \xi_2$, $\xi_{1,2} = \left(-\eta_d \pm \xi\right)/2$, $\xi = \sqrt{\eta_d^2 - 4\sigma^2}$, $\sigma^2 = E^2\sigma_g\sigma_{-g}$, $\varepsilon_{1,2} = \sigma_0 + i\psi + \xi_{1,2}$, $\eta_d = \eta + i2\psi$, $\psi = \sigma_g\sigma_{-g}\left(1 - E^2\right)\tau$, $\eta = 2\pi\left[\chi_0 + \Delta\theta\sin\left(2\theta_0\right)\right]/\left(\lambda\gamma_0\right)$, $\sigma_0 = \pi\chi_0/\left(\lambda\gamma_0\right)$, $\sigma_{\pm g} = \chi_{\pm g}c/\left(\lambda\left|\gamma_{g,0}\right|\right)$. Here, *E* is the static Debye–Waller (D-W) factor, λ – X-ray wavelengths, γ_0 and γ_g are direction cosines, χ_0, χ_g, χ_{-g} – electric susceptibilities, which are related to the structure factor of the crystal unit cell, *c* is the polarization factor, θ – angle of incidence, θ_0 – Bragg angle, $\Delta\theta = \theta - \theta_0$ – deviation from the exact Bragg position.

The X-ray diffraction spectra from the $Al_xGa_{1-x}N$/GaN heterostructures were calculated using the recursive formula approach. Accordingly, the amplitude coefficients of reflected R_n and transmitted T_n waves in the *n*-th layer of a multilayered system are given as follows [11]:

$$R_n^g = r_n^g + \frac{t_n t_n^{-g} R_{n-1}^g}{1 - R_{n-1}^g r_n^{-g}}\,,\ T_n = \frac{T_{n-1}t_n}{1 - R_{n-1}^g r_n^{-g}}\,. \tag{6}$$

In more details, to obtain the diffracted intensity, the $Al_xGa_{1-x}N$/GaN heterostructure is first separated by *n* sublayers. Then, this calculation starts from the substrate, and the recursion equations are used successively for each sublayer until the surface of the sample. Finally, the coherent part of the diffracted intensity is given by:

$$I_g^c = \left|R_n\right|^2. \tag{7}$$

Reduction of diffracted intensity due to displacement fields $\langle u\rangle$ associated with microdefects is accounted by using the static Debye–Waller factor *E* [11, 13, 14]:

$$E = \left\langle\exp\left(i\vec{g}\delta\vec{u}\right)\right\rangle, \tag{8}$$

where $\vec{g}$ is the diffraction vector.

The randomly distributed spherically symmetric defects, which have zero deformation fields outside the cluster [11, 14–16], are considered to generalize the types of point defects and to describe the microdefect structure of the ion-implanted samples.

The displacement field for randomly distributed spherically symmetric defects [11, 14–16] is given by:

$$\delta\vec{u}(r)=\begin{cases} 0, \text{ if } |\vec{r}|>R_d \\ \text{random value, if } |\vec{r}|\le R_d \end{cases} \quad (9)$$

The concentration of point defects in the $Al_xGa_{1-x}N$ layers implanted with Ar^+ ions is commonly higher than in GaN bulk material [17, 18], and for the mentioned implantation energy and doses is expected to be at the order of 10^{19} cm^{-3} [19, 20].

Then, the static D-W factor is given by [11,14,16]:

$$E=\exp\left(-C_d\frac{4\pi}{3}R_d^3\right) \quad (10)$$

and, for low defect concentrations E is reduced to [16]:

$$E=1-C_d\frac{4\pi}{3}R_d^3. \quad (11)$$

Here, C_d and R_d are the concentration and microdefect radius, respectively.

The correlation length τ is the main parameter of statistical theory of X-ray diffraction, which determines the defect related diffuse scattering [11, 14, 15]:

$$\tau=\int_0^\infty \exp(i\eta\varsigma)g(\varsigma)d\varsigma, \quad (12)$$

where $g(\varsigma)$ is the correlation function [11, 13, 16].

In general, there are few types of spherical-symmetric microdefects, each requiring unique expressions for the correlation functions [13, 14, 16]. In this work, for the sake of simplicity the correlation function was generalized by the Gaussian function [13, 16]:

$$g(\varsigma)=\exp\left(\frac{\pi\varsigma^2}{4\tau_0}\right), \quad (13)$$

which leads to the correlation length in the form of [13, 15]:

$$\tau=\tau_0\exp\left(-y^2\right)\cdot\left[1+erf(iy)\right], \quad (14)$$

where $y=\tau_0\eta/\sqrt{\pi}$ and τ_0 is the Kato correlation length [21].

Considering the mentioned above spherically symmetric defects, the following relation is obtained between the correlation length τ_0 and defect radius R_d [14, 15]:

$$\tau_0=\frac{3}{4}R_d\gamma_0, \quad (15)$$

where $\gamma_0=\sin(\theta_0)$.

Also, taking into account Eqs. (11) and (15), the defect radius (R_d) and concentration of defects (C_d) can be determined as follows:

$$R_d=\frac{4}{3}\frac{\tau_0}{\sin(\theta_0)}, \quad (16)$$

$$C_d=\frac{81}{64}\frac{(\sin(\theta_0))^3\cdot(1-E)}{\pi\tau_0^3}. \quad (17)$$

Finally, within the kinematical approximation, the diffuse part of the diffracted intensity is given by [13, 15]:

$$I_g^d=2\left|\sigma_g\right|^2\left(1-E^2\right)\cdot\mathrm{Re}(\tau)\cdot l. \quad (18)$$

4. Results and discussion

The reciprocal space maps (RSMs) were measured around the asymmetrical ($20\bar{2}5$) reflection to study the epitaxial relationship in the ion-implanted $GaN/Al_xGa_{1-x}N$ heterostructures after implantation and annealing processing. The ($20\bar{2}5$) RSMs of samples S1 and S2 are shown in Figs. 1a-d and Figs. 1e-h, respectively. The Q_x coordinate is inversely related to the lattice parameter a and Q_z – to the parameter c on RSMs. The most intensive peak and the elongated vertical streaks above it are attributed to the undamaged part of the GaN substrate and the compositionally graded $Al_xGa_{1-x}N$ layer, respectively. Implantation with Ar^+ ions introduces expansion of the lattice parameter c, which is reflected in a downward shift of both the $Al_xGa_{1-x}N$ peaks and streak below the GaN peak (Figs. 1b, 1c, 1f and 1g). The second implantation has induced an extra downward Q_z shift only for the $Al_xGa_{1-x}N$ peaks (Fig. 1c and 1g), which means increasing of the lattice parameter c. In addition, RSMs shows fully strained graded layer to GaN substrate at all the processing stages. Also, after each processing stage, there are no visible Q_x shift of the $Al_xGa_{1-x}N$ and GaN peak position, which indicates that implantation does not introduce notable strain along the a-axis of the crystal lattice. It is in agreement with previous reports [8, 22–24]. The high-temperature annealing resulted in a remarkable lattice recovery; however, some residual c-lattice extension is still observed in both the GaN and $Al_xGa_{1-x}N$ layers (Fig. 1d and 1h).

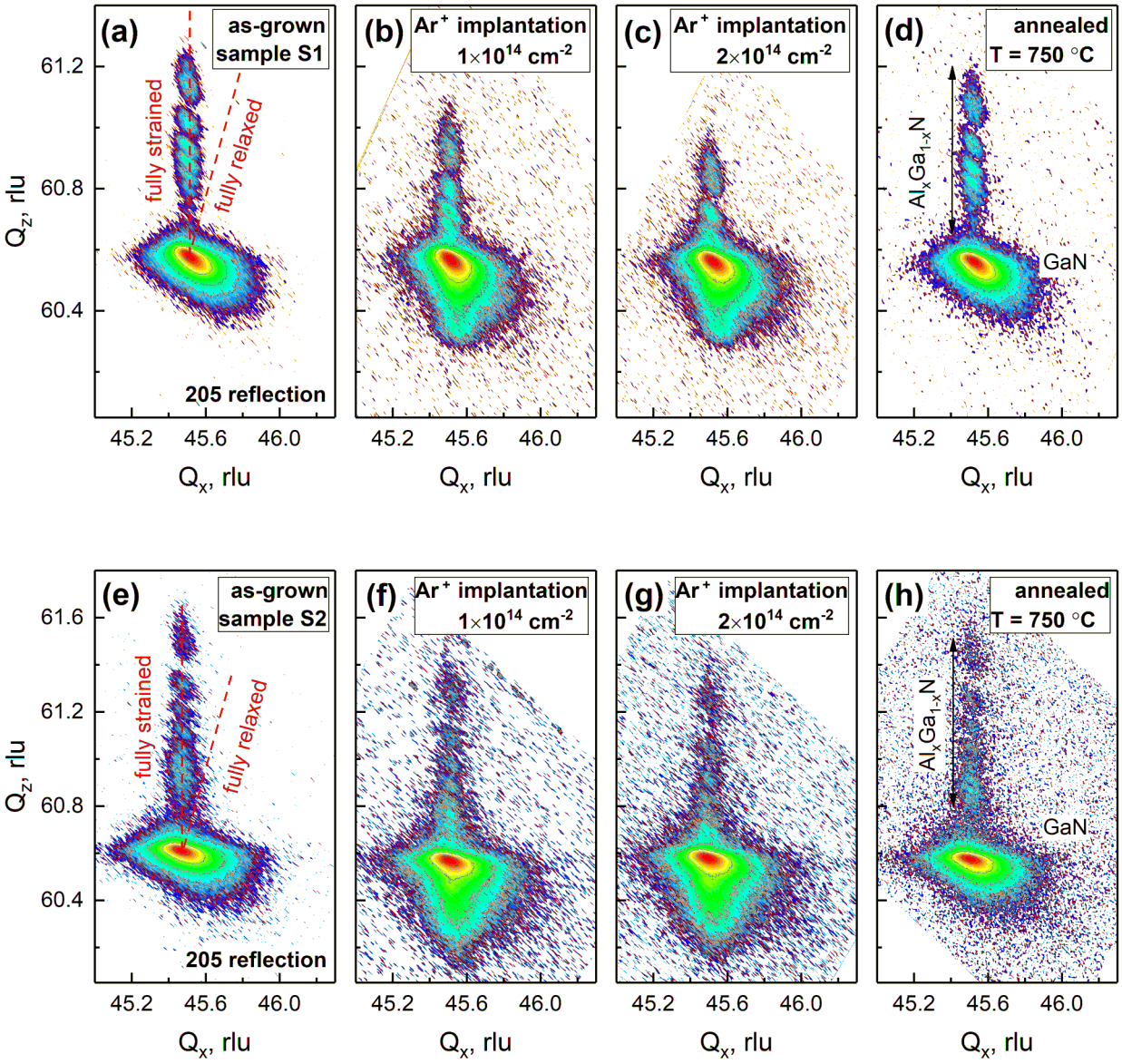

Fig. 1. ($20\bar{2}5$) RSMs of the samples S1 (*a*-*d*) and S2 (*e*-*h*) measured at the different processing stage: (*a*, *e*) as-grown, (*b*, *f*) after the first implantation, (*c*, *g*) after the second implantation, and (*d*, *h*) after the high-temperature annealing.

The HRXRD 2θ/ω scans were measured around the symmetrical (0002) reflection to investigate in more details the implantation damage in the compositionally graded layers. The scattered intensity near the low-order reflection is generally characterized with higher intensity contrast between the interference fringes and background level, which is important for retrieving reliable data. For the samples S1 and S2, the measured (grey circles) (0002) 2θ/ω scans are shown in Fig. 2. The most intense peak on the HRXRD spectra corresponds to the undamaged GaN substrate. The peaks from the graded $Al_xGa_{1-x}N$ layer appear in the form of interference fringes at the right side of the sharp GaN peak. Ion-implantation resulted in an extension of the GaN and $Al_xGa_{1-x}N$ peaks toward the lower angles, which is almost fully recovered after the high-temperature annealing. Since the extension at the left side of the GaN peak also vanishes, this additionally confirms its strain nature. The (0002) 2θ/ω scans were simulated to compare the strain in the $Al_xGa_{1-x}N$/GaN heterostructures after the implantation with different Ar^+ doses.

The depth profiles of Al concentration in the $Al_xGa_{1-x}N$ layers of the as-grown samples S1 and S2 (insets in Fig. 2) were previously determined in Ref. [10] and are used in this work to study the effect of ion implantation on the strain distribution in the $Al_xGa_{1-x}N$/GaN heterostructures. It is well known that ion implantation is accompanied with formation of a high density of point defects, which generally leads to a vertical hydrostatic expansion of the unit cell (Fig. 1). To simulate 2θ/ω scans, the hydrostatic strain in the $Al_xGa_{1-x}N$ and GaN buffer layers was approximated with

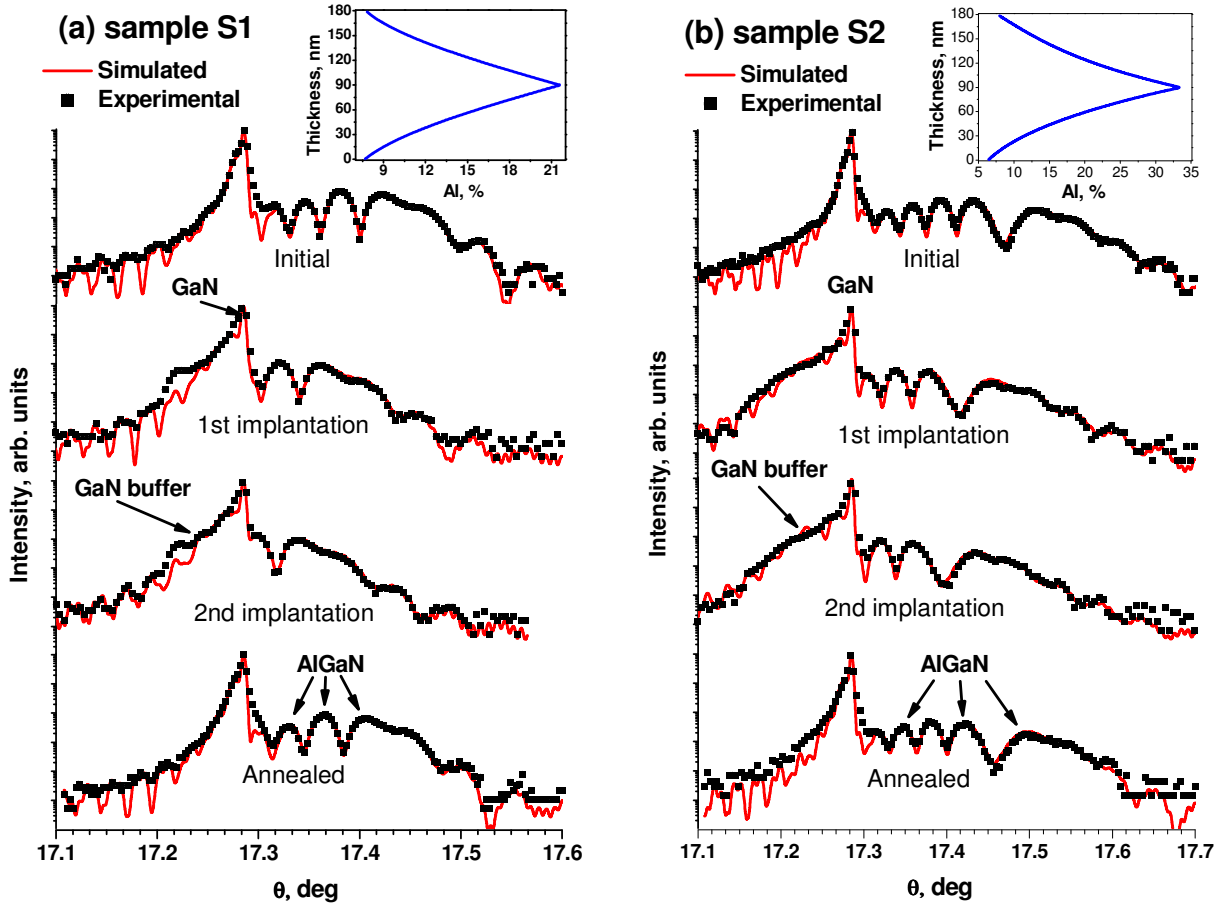

Fig. 2. Measured (gray circles) and simulated (red lines) (0002) 2θ/ω scans of the samples S1 (a) and S2 (b). The insets show the depth profiles of Al concentration in the $Al_xGa_{1-x}N$ layers of samples S1 and S2.

the two-piece normal distribution (Eq. (19)), which is often used to fit the strain distribution in the ion-implanted layers [25], and an exponential function (Eq. (20)), respectively:

$$\left(\frac{\Delta d}{d}\right)_{\mathrm{AlGaN}} = T\exp\left[-\left(\frac{z-\rho}{2\Omega_i}\right)^2\right],\ i=\begin{cases}1, & z\le\rho\\ 2, & z>\rho\end{cases} \tag{19}$$

$$\left(\frac{\Delta d}{d}\right)_{\mathrm{GaN}} = k_1\exp(-k_2 z). \tag{20}$$

Here, ρ is the implanted range, Ω_1 and Ω_2 are the left- and right-hand-side standard deviations, T is the peak strain value, k_1 and k_2 are fitting parameters, and z is the distance from the sample surface.

The differential evolution method [27, 28] allows one to minimize the deviation between two profiles and was employed for XRD 2θ/ω scans fitting. The error between the experimental and calculated 2θ/ω scans was determined as in Refs. [29, 30]. For the samples under investigation, the fitting is additionally complicated by the low intensity of the fringes from the $Al_xGa_{1-x}N$ layer and the relatively high intensity from the peak at the lower angles from the GaN substrate.

The widely used minimization criteria, such as mean-absolute error [27], relative error [27], and those described in Refs. [31–33], does not allow a good fitting of the entire XRD 2θ/ω scan, which is even more complicated when considering the diffuse scattering. Therefore, we first fitted the part of the 2θ/ω scan associated with the $Al_xGa_{1-x}N$ layer, assuming the strain profiles, the static D-W factor, and the Kato correlation length in the form of two-sided Gaussian functions similar to those for the strain distribution (Eq. (19)). The profiles of the static Debye–Waller factor and the Kato correlation length were characterized with a common maximum. Second, the fitting criterion between the measured and simulated spectra is given as follows [30]:

$$Err = \frac{1}{N}\sum_N \left|I_{\mathrm{exp}} - I_{\mathrm{calc}}\right|^K, \tag{21}$$

where the user specified value of K is limited within [0.1–0.9]. For small and large values of K, a good fitting is achieved for the low and high intensity features of the 2θ/ω scan, respectively. When using the abovementioned

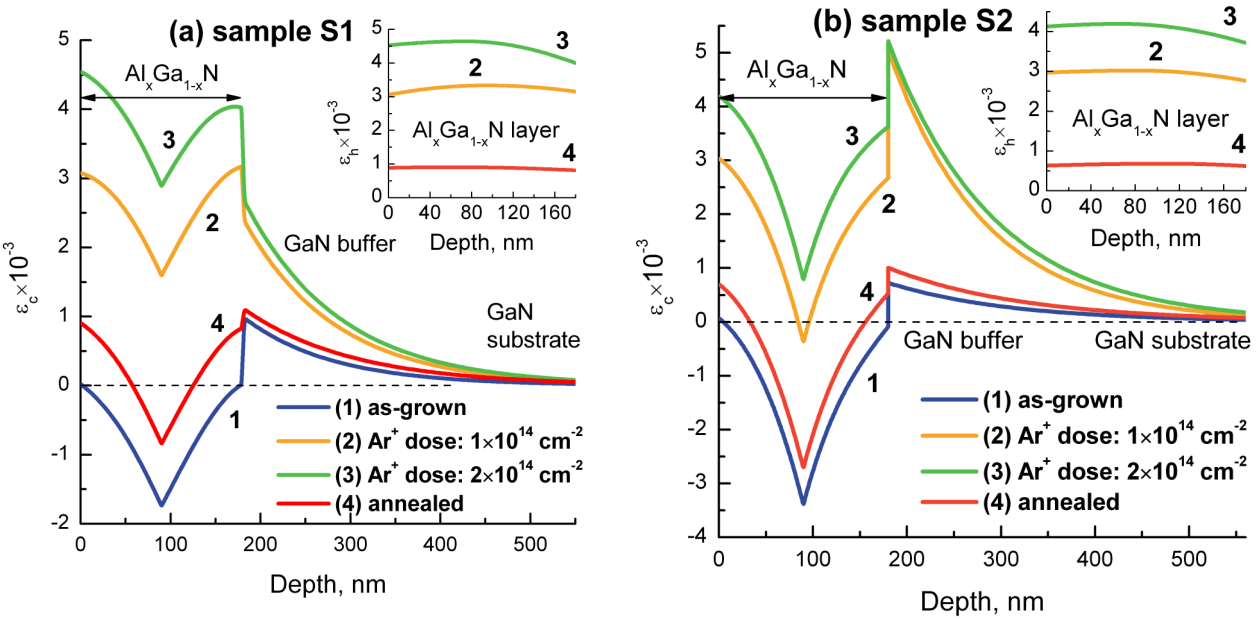

Fig. 3. The depth profiles of strain in the samples S1 (a) and S2 (b). The inset shows the hydrostatic strain in the $Al_xGa_{1-x}N$ layers after the implantation and annealing processes.

criteria [27] with $K = 1$ and $K = 2$, the best fit is achieved near the peak of the GaN substrate, where the intensity is high. However, the fitting of the $Al_xGa_{1-x}N$ layer is generally poor. Therefore, the $Al_xGa_{1-x}N$ peak was first fitted separately, using $K \approx [0.5-0.65]$, while the parameters k_1 and k_2 in (Eq. (20)) were kept fixed. After this, the determined fitting parameters for the $Al_xGa_{1-x}N$ layer were fixed, and the peak for the GaN buffer layer was fitted by changing k_1 and k_2 in Eq. (20). For the GaN buffer, the values of K were given both larger [0.7–0.8] and lower [0.2–0.5] than for the $Al_xGa_{1-x}N$ layer. The mutual influence of small changes in the fitting parameters of the two-step fitting process on the XRD spectra is small and can be neglected.

The deviation between the experimental and calculated XRD spectra is estimated using the following relative error:

$$Err_{rel} = \frac{1}{N}\sum_{N}\frac{\left|I_{\exp} - I_{calc}\right|}{I_{\exp}} \qquad (22)$$

The relative error of the performed fitting did not exceed 40% for the sample S1 and 48% for the sample S2.

The depth profiles of strain in the $Al_xGa_{1-x}N$/GaN heterostructures obtained from the simulations are shown in Fig. 3. The $Al_xGa_{1-x}N$ layers of the as-grown samples are under compressive strain (ε_c) along the c-axis due to the tensile biaxial strain (ε_a) in the (0001) basal plane induced by the constant in-plane lattice parameter. The observed jump of ε_c at the $Al_xGa_{1-x}N$/GaN interface results from the fact that the grading of Al concentration in the $Al_xGa_{1-x}N$ layer starts from about 7%, resulting in the ~0.17% lattice misfit at the $Al_xGa_{1-x}N$/GaN interface. After the implantation, an almost uniform depth distribution of hydrostatic strain in the $Al_xGa_{1-x}N$ layers the most correctly describes the $Al_xGa_{1-x}N$ peaks on the (0002) 2θ/ω scan. This is despite the high implantation energy (100 keV) that should have resulted in the maximum concentration of Ar^+ at the depth of about 90 nm from the surface [19], which is often reported for ion implantation into single crystals [26]. The strain in the GaN buffer increases only after the implantation with the first dose of Ar^+ ions and is not affected by the second dose. Like to that in the $Al_xGa_{1-x}N$ layer, the strain in the GaN buffer is almost totally reduced after the sample annealing.

Fig. 4 shows the averaged over the sample area depth profiles of the static Debye–Waller factor (E) and of the Kato correlation length (τ_0) for the sample S1. The shape of these profiles is very close to that of the demonstrated in Fig. 3 (inset) hydrostatic strain. The detailed analysis of the XRD spectra inherent to the samples S1 and S2 suggest the presence of few types of microdefects. For example, the microdefects of small and large radius have a dominant effect on the spectra tail far and close to the Bragg position, respectively [34]. However, consideration of more types of microdefects sufficiently complicates the XRD spectra fitting and interpretation of results. Therefore, we consider only one dominant type of microdefects, which is characterized with some averaged across the layer parameters of the D-W factor, correlation length, as well as their depth distribution.

Fig. 5 shows the microdefects radii and concentrations, which were calculated according to Eqs. (16) and (17) and averaged over the compositional gradient layer thickness. A higher concentration of defects with smaller radius is seen by comparing the

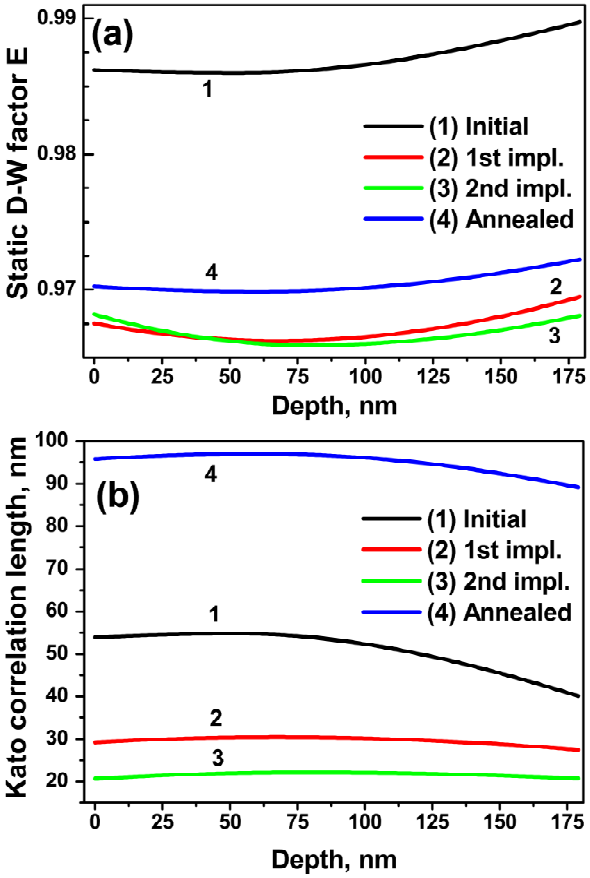

Fig. 4. Depth profiles of the static Debye–Waller factor E (a) and Kato correlation length τ_0 (b) for the sample S1.

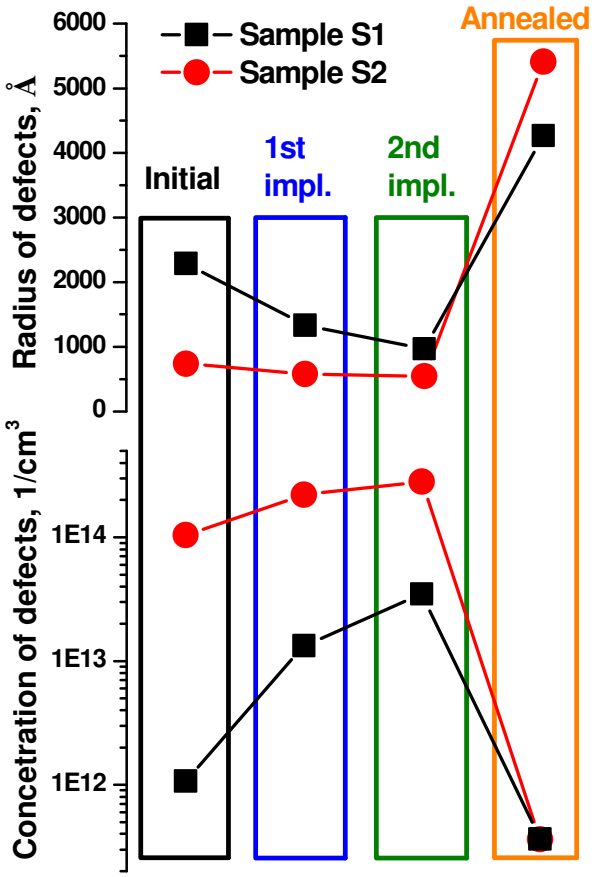

Fig. 5. The average defect radius R_d and concentration of defects C_d in the AlGaN layers of the samples S1 and S2 after the growth, implantation and annealing stages.

as-grown samples S2 and S1, which can be explained by the higher Al concentration in the $Al_xGa_{1-x}N$ layer of the sample S2. After ion implantation, the average defect size decreases with simultaneous increase of the defect concentration, and which is most noticeably observed for the sample S1. It should be noted that due to the high crystalline quality of the samples S1 and S2, the coherent part of diffracted intensity dominates over the diffuse component, which reduces the accuracy of determined depth profiles of the static D-W factor and radii of defects [35]. After the high-temperature annealing, the average microdefect size increases sufficiently. Also, for both samples the average concentration of defects is almost the same and lower than for the as-grown sample.

III-nitride heterostructures are commonly characterrized with a high density of dislocations (10^8–10^{10} cm^{-2}), and the effect of dislocations is higher for XRD spectra measured for high-order reflections. To simulate XRD spectra for investigated ion-implanted structures, the dislocations were included into the static Debye–Waller factor along with the point defects. However, for simplicity it was assumed that the diffuse scattering was caused solely by point defects. Moreover, the dislocations broadening of (0002) 2θ/ω scans is small in comparison with high-order reflections [29]. This also explains the weaker change of the microdefect state of the sample S2 in comparison with the sample S1. The defect concentration in the as-grown sample S2 is higher due to the higher Al concentration in the $Al_xGa_{1-x}N$ layer, and higher lattice mismatch [10].

For perfect single crystals, the high-temperature processes, such as annealing, lead to generation of dislocation loops and defect agglomeration. However, for highly-dislocated crystals, the high-temperature annealing causes changes in dislocation configuration and their gliding with simultaneous change of the microdefect concentration [36, 37].

The triple-crystal (0002) ω-scans were measured at the Bragg positions of the GaN substrate and $Al_xGa_{1-x}N$ layer to additionally study the type of defects introduced by ion implantation. Fig. 6 compares the double logarithmic plots of the (0002) ω-scans for the initial and Ar^+-implanted sample S2. The broadening normal to the diffraction vector reflects the defect structure of the sample and for high-quality crystalline materials is determined by instrumental factors. Commonly, the slope of line shapes at the tail region follows the power law $I \sim \Delta\theta^{-n}$ for both ω and 2θ/ω scan types. Depending on the type of defects, n can vary between 2 and 5. Thereby, for epitaxial layers containing ordered threading dislocations, the double-crystal and triple-crystal measurements shows $n = 3$ and $n = 4$, respectively [38]. This was previously theoretically calculated by Kryvoglaz and then developed in the works of Kaganer

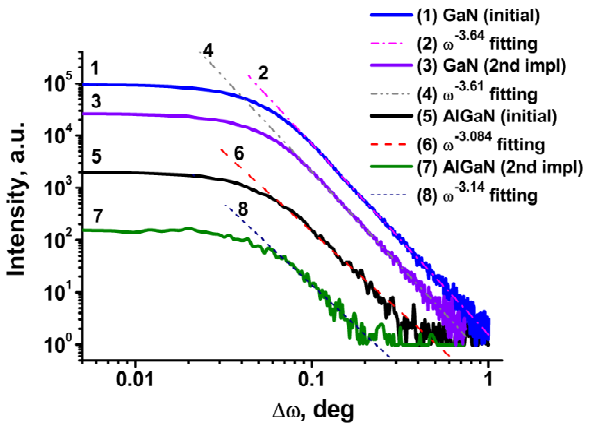

Fig. 6. Triple-crystal (0002) ω-scans in the log-log scale measured for GaN substrate, and $Al_xGa_{1-x}N$ layer for the initial state and after the second stage of implantation in the sample S2.

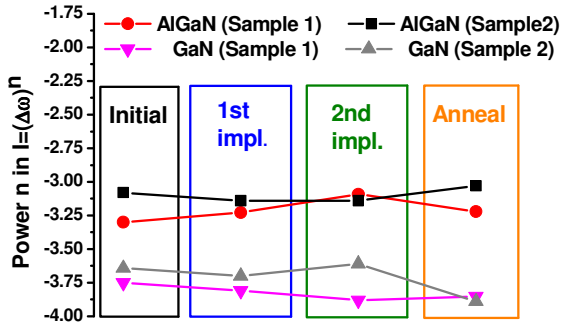

Fig. 7. The slope of the tail region determined from the (0002) ω-scans of GaN buffer and AlGaN layer from the samples S1 and S2.

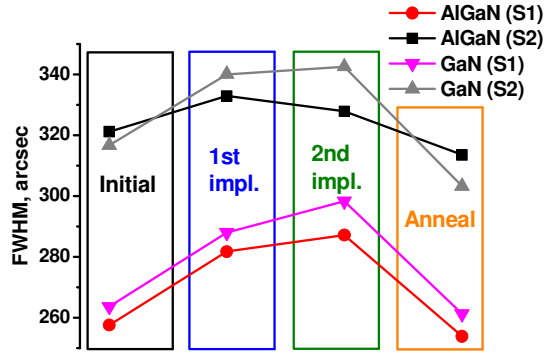

Fig. 8. FWHM of the (0002) ω-scans measured for the $Al_xGa_{1-x}N$ layers and GaN substrates of the samples S1 and S2.

et al. [39]. Additionally, Barchuk *et al*. [40] have shown that *n* can vary between 2 and 3, depending on the type of threading dislocations (screw or edge).

For epitaxial layers containing random dislocations, the intensity decay at the tail region of the (0002) ω-scan is generally faster than for layers with threading pure screw dislocations [38]. It should be mentioned that for high densities of dislocations the behavior of intensity decay does not depends on the dislocations density but is defined solely by the dislocation type [38]. Additionally, due to the high densities of dislocations in as-growth non-implanted III-nitrides, the influence of point defects on the intensity decay is commonly neglected.

The slope of the tail region determined from the (0002) ω-scans of the samples S1 and S2 are plotted in Fig. 7. It can be seen that the slope of the intensity decay for the GaN template is about 3.75…3.88 for the sample S1 and about 3.6…3.8 for the sample S2, and only slightly changes after the high-temperature annealing. The slope for the $Al_xGa_{1-x}N$ layer is about 3.25 and 3.05 for the samples S1 and S2. The slope is only slightly affected by the implantation and annealing processes. Therefore, it may be concluded that the ion implantation does not sufficiently affect the dislocation configuration of the $Al_xGa_{1-x}N$/GaN heterostructure.

The full width of half maximum (FWHM) of ω-scans for symmetrical (0002) reflection is commonly measured to estimate the density of screw-type dislocations [10]. FWHMs for the $Al_xGa_{1-x}N$ layers and GaN substrates of the samples S1 and S2 are shown in Fig. 8, and compared for the as-grown, ion-implanted, and annealed stages. It can be seen that the density of screw-type dislocation is lower in the GaN and $Al_xGa_{1-x}N$ layers of the sample S1, which has a lower Al concentration in the $Al_xGa_{1-x}N$ layer. The density of screw-type dislocations in the $Al_xGa_{1-x}N$ layers is about $1.35 \cdot 10^8$ cm^{-2} and $2.1 \cdot 10^8$ cm^{-2} for the samples S1 and S2, respectively [10]. FWHM increases after the first implantation and only slightly – after the second implantation step. The increase of the dislocation density at room temperature is unlikely, and the increase of the FWHM is probably related with the increase of the concentration of point defects and the change of the strain state in the sample. FWHM sufficiently decreases after the high-temperature annealing, which indicate the reduced concentration of point defects induced by implantation and small changes in the dislocation concentration. The nature of broadening of the GaN substrate peak is different from that of the $Al_xGa_{1-x}N$ layer. It was shown in Ref. [19] that implantation in the upper part of an AlN/GaN SL also leads to an increase of the defect concentration in the buffer layer, which can be explained by the strain and microdefects redistribution in the sample. This also can be attributed to the samples S1 and S2 to explain the ω-scan broadening by the strain distribution and defect migration in the Al_2O_3-GaN substrate-GaN buffer-compositional gradient layer.

5. Conclusions

In this work, the compositionally graded $Al_xGa_{1-x}N$/GaN heterostructures were implanted with Ar^+ ions to study the possibility of strain engineering. A method was developed to retrieve the profiles of strains and those of the fluctuational displacements of atoms caused by the presence of microdefects in a crystalline film by

simulating the XRD spectra from the ion-implanted heterostructures with including the diffuse scattering. It was shown that ion implantation with doses and energy of about $(1…2)\cdot10^{14}$ cm^{-2} and 100 keV does can induce large values of hydrostatic strain ~0.3…0.46% and relatively low damage of the crystalline lattice. Ion implantation influences mainly on the density of point defects, while the dislocation configuration is almost unaffected. The density of microdefects is sufficiently reduced after the post-implantation annealing facilitated.

The structural perfection of the $Al_xGa_{1-x}N$ layers strongly depends on the Al concentration, and is reduced with increased Al. The structural changes induced by ion implantation in highly defected samples are less pronounced. Ion-implantation leads to ω-scans broadening from both the $Al_xGa_{1-x}N$ and GaN layers, which can be explained by migration of the point defects and redistribution of strain fields within the heterostructure. Due to the high density of dislocations in III-nitrides, the microdefect structure can be better distinguished for the ion-implanted samples with ultra-low density of dislocations.

References

1. Jena D., Heikman S., Green D., Buttari D., Coffie R., Xing H., Keller S., DenBaars S., Speck J.S., Mishra U.K. and Smorchkova I. Realization of wide electron slabs by polarization bulk doping in graded III-V nitride semiconductor alloys. *Appl. Phys. Lett*. 2002. **81**, No. 23. P. 4395–4397. doi: 10.1063/1.1526161.
2. Simon J., Protasenko V., Lian C., Xing H. and Jena D. Polarization-induced hole doping in wide-band-gap uniaxial semiconductor heterostructures. *Science*. 2010. **327,** P. 60–64. doi: 10.1126/science.1183226.
3. Li S., Ware M., Wu J., Minor P., Wang Z., Wu Z., Jiang Y. and Salamo G. J. Polarization induced pn-junction without dopant in graded AlGaN coherently strained on GaN. *Appl. Phys. Lett.* 2012. **101**, No. 12. P. 122103. doi: 10.1063/1.4753993.
4. Tadjer M.J., Feigelson B.N., Greenlee J.D., Freitas J.A., Anderson T.J., Hite J.K., Ruppalt L., Eddy C.R., Hobart K.D. and Kub F.J. Selective *p*-type doping of GaN:Si by Mg ion implantation and multicycle rapid thermal annealing. *ECS J. Solid State Sci. Technol.* 2016. **5**, No. 2. P. 124–127. doi: 10.1149/2.0371602jss.
5. Liu C., Mensching B., Volz K. and Rauschenbach B. Lattice expansion of Ca and Ar ion implanted GaN. *Appl. Phys. Lett*. 1997. **71**, No. 16. P. 2313–2315. doi: 10.1063/1.120059.
6. Liu C., Mensching B., Zeitler M., Volz K. and Rauschenbach B. Ion implantation in GaN at liquid-nitrogen temperature: Structural characteristics and amorphization. *Phys. Rev. B.* 1998. **57**, No. 4. P. 2530–2535. doi: 10.1103/PhysRevB.57.2530.
7. Pagowska K., Ratajczak R., Stonert A., Nowicki L. and Turos A. Compositional dependence of damage buildup in Ar-ion bombarded AlGaN. *Vacuum*. 2009. **83**. P. S145–S147. doi: 10.1016/j.vacuum.2009.01.048.
8. Fialho M., Magalhães S., Chauvat M. P., Ruterana P., Lorenz K. and Alves E. Impact of implantation geometry and fluence on structural properties of $Al_xGa_{1-x}N$ implanted with thulium. *J. Appl. Phys*. 2016. **120**, No. 16. P. 165703. doi: 10.1063/1.4966120.
9. Faye D.N., Alves E., Felizardo M., Wendler E., Brunner F., Lorenz K., Magalhães S. and Weyers M. Mechanisms of implantation damage formation in $Al_xGa_{1-x}N$ compounds. *J. Phys. Chem. C*. 2016. **120**, No. 13. P. 7277–7283. doi: 10.1021/acs.jpcc.6b00133.
10. Kuchuk A.V., Lytvyn P.M., Li C., Stanchu H.V., Mazur Y.I., Ware M.E., Benamara M., Ratajczak R., Dorogan V., Kladko V.P., Belyaev A.E. and Salamo G.G. Nanoscale electrostructural characterization of compositionally graded $Al_xGa_{1-x}N$ heterostructures on GaN/sapphire (0001) substrate. *ACS Appl. Mater. Interfaces.* 2015. **7**, No. 41. P. 23320–23327. doi: 10.1021/acsami.5b07924.
11. Punegov V.I. X-Ray diffraction from multilayer structures with statistically distributed microdefects. *phys. status solidi* (*a*). 1993. **136**, No. 1. P. 9–19. doi: 10.1002/pssa.2211360102.
12. Punegov V.I. Dynamic X-ray diffraction in layered-inhomoneous systems. *Tech. Phys. Lett.* 1994. **20**, No. 1. P. 58–59.
13. Punegov V.I., Petrakov A.P. and Tikhonov N.A. X-ray diffraction on laser disturbed near-surface crystal layers. *phys. status solidi* (*a*). 1990. **122**, No. 2. P. 449–458. doi: 10.1002/pssa.2211220202.
14. Pavlov K.M. and Punegov V.I. Der einfluß kugelsymmetrischer kristalldefekte auf die winkelverteilung gebeugter röntgenstrahlung. *phys. status solidi* (*a*). *Basic Res.* 1997. **199**, No. 1. P. 5–14. doi: 10.1002/1521-3951(199701)199:1<5::AID-PSSB5>3.0.CO;2-V.
15. Punegov V.I. and Pavlov K.M. Models of spherically symmetric microdefects in the statistical dynamical theory of diffraction: II. Correlation length. *Crystallogr. Reports.* 1996. **41**, No. 4. P. 585–591.
16. Punegov V.I. and Pavlov K.M. Models of Spherically Symmetric Microdefects in the Statistical Dynamical Theory of Diffraction: I. Correlation Function. *Crystallogr. Reports.* 1996. **41**, No. 4. P. 575–584.
17. Boguslawski P., Briggs E.L. and Bernholc J. Native defects in gallium nitride. *Phys. Rev. B.* 1995. **51**, No. 23. P. 17255–17258. doi: 10.1103/PhysRevB.51.17255.
18. Fehrer M., Einfeldt S., Birkle U., Gollnik T. and Hommel D. Impact of defects on the carrier transport in GaN. *J. Cryst. Growth.* 1998. **189–190**. P. 763–767. doi: 10.1016/S0022-0248(98)00284-X.

19. Liubchenko O.I., Sabov T.M., Kladko V.P., Melnik V.P., Yukhymchuk V.O., Romaniuk B.M., Kolomys O., Hreshchuk O., Dubikovskyi O.V., Maksymenko Z.V., Gudymenko O.Yo. and Belyaev A.E. Modification of elastic deformations and analysis of crystalline changes in Ar^+-implanted AlN/GaN superlattices. *Appl. Nanosci.* 2019. **9**. doi: 10.1007/s13204-019-01000-w.
20. Ziegler J.F., Ziegler M.D. and Biersack J.P. SRIM – The stopping and range of ions in matter (2010). *Nucl. Instruments Methods Phys. Res. Sect. B Beam Interact. with Mater. Atoms*. 2010. **268**, No. 11-12. P. 1818–1823. doi: 10.1016/j.nimb.2010.02.091.
21. Kato N. Statistical dynamical theory of crystal diffraction. I. General formulation. *Acta Crystallogr. Sect. A.* 1980. **36**, No. 5. P. 763–769. doi: 10.1107/S0567739480001544.
22. Pipeleers B., Hogg S. M. and Vantomme A. Defect accumulation during channeled erbium implantation into GaN. *J. Appl. Phys.* 2005. **98**, No. 12. P. 123504. doi: 10.1063/1.2143120.
23. Fialho M., Rodrigues J., Magalhães S., Correia M. R., Monteiro T., Lorenz K. and Alves E. Effect of AlN content on the lattice site location of terbium ions in $Al_xGa_{1-x}N$ compounds. *Semicond. Sci. Technol.* 2016. **31**, No. 3. P. 035026. doi: 10.1088/0268-1242/31/3/035026.
24. Magalhães S., Fialho M., Peres M., Lorenz K. and Alves E. Quantitative x-ray diffraction analysis of bimodal damage distributions in Tm implanted $Al_{0.15}Ga_{0.85}N$. *J. Phys. D. Appl. Phys.* 2016. **49**, No. 13. P. 135308. doi: 10.1088/0022-3727/49/13/135308.
25. Klappe J.G.E. and Fewster P.F. Fitting of rocking curves from ion-implanted semiconductors. *J. Appl. Crystallogr.* 1994. **27**. P. 103–110. doi: 10.1107/S0021889893007484.
26. Arulkumaran S., Kennedy J., Bhat T.N., Ng G.I., Ranjan K., Tripathy S. and Murmu P.P. Thermally stable device isolation by inert gas heavy ion implantation in AlGaN/GaN HEMTs on Si. *J. Vac. Sci. Technol. B, Nanotechnol. Microelectron. Mater. Process. Meas. Phenom.* 2016. **34,** No. 4. P. 042203. doi: 10.1116/1.4955152.
27. Wormington M., Panaccione C., Matney K.M. and Bowen D.K. Characterization of structures from X-ray scattering data using genetic algorithms. *Philos. Trans. R. Soc. A Math. Phys. Eng. Sci.* 1999. **357**, N 1761. P. 2827–2848. doi: 10.1098/rsta.1999.0469.
28. Storn R. and Price K. Differential evolution – a simple and efficient heuristic for global optimization over continuous spaces. *J. Glob. Optim.* 1997. **11**, No. 4. P. 341–359. doi: 10.1023/A:1008202821328.
29. Liubchenko O.I., Kladko V.P., Sabov T.M. and Dubikovskyi O.V. X-ray analysis for micro-structure of AlN/GaN multiple quantum well systems. *J. Mater. Sci. Mater. Electron.* 2019. **30**, No 1. P. 499–507. doi: 10.1007/s10854-018-0315-3.
30. Liubchenko O.I. and Kladko V.P. Simulation of X-ray diffraction spectra for AlN/GaN multiple quantum well structures on AlN(0001) with interface roughness and variation of vertical layers thickness. *Metallofiz. i Noveishie Tekhnologii.* 2018. **40**, No. 6. P. 759–776. doi: 10.15407/mfint.40.06.0759.
31. Boulle A. and Debelle A. Strain-profile determination in ion-implanted single crystals using generalized simulated annealing. *J. Appl. Crystallogr.* 2010. **43**, No. 5. P. 1046–1052. doi: 10.1107/S0021889810030281.
32. Zolotoyabko E. Extended kinematic approach to the simulation of high-resolution X-ray diffraction spectra. Application to structures with buried amorphous layers. *J. Appl. Crystallogr.* 1998. **31**, No. 2. P. 241–251. doi:10.1107/S0021889897009096.
33. Liubchenko O., Kladko V. and Gudymenko O. Yo. Modeling of X-ray rocking curves for layers after two-stage ion-implantation. *Semicond. Physics, Quantum Electron. Optoelectron.* 2017. **20**, No. 3. P. 355–361. doi: 10.15407/spqeo20.03.355.
34. Kladko V.P., Datsenko L.I., Bak-Misiuk J., Olikhovskii S.I., Machulin V.F., Prokopenko I.V., Molodkin V.B. and Maksimenko Z.V. Calculation of two-dimensional maps of diffuse scattering by a real crystal with microdefects and comparison of results obtained from three-crystal diffractometry. *J. Phys. D. Appl. Phys.* 2001. **34**, No. 10A. P. A87–A92. doi: 10.1088/0022-3727/34/10A/318.
35. Shcherbachev K.D., Bublik V.T., Mordkovich V.N. and Pazhin D.M. Specific features of formation of radiation defects in the silicon layer in "silicon-on-insulator" structures. *Semiconductors.* 2011. **45**, No. 6. P. 738–742. doi: 10.1134/S1063782611060224.
36. Moram M.A., Sadler T.C., Häberlen M., Kappers M.J. and Humphreys C.J. Dislocation movement in GaN films. *Appl. Phys. Lett.* 2010. **97**, No. 26. P. 261907. doi: 10.1063/1.3532965.
37. Iwata H., Kobayashi H., Kamiya T., Kamei R., Saka H., Sawaki N., Irie M., Honda Y. and Amano H. Annealing effect on threading dislocations in a GaN grown on Si substrate. *J. Cryst. Growth.* 2017. **468**. P. 835–838. doi: 10.1016/j.jcrysgro.2017.01.001
38. Kyutt R.T. Defect structure of epitaxial layers of III nitrides as determined by analyzing the shape of X-ray diffraction peaks. *Tech. Phys.* 2017. **62**, No. 4. P. 598–603. doi: 10.1134/s1063784217040144
39. Kaganer V.M., Brandt O., Trampert A. and Ploog K.H. X-ray diffraction peak profiles from threading dislocations in GaN epitaxial films. *Phys. Rev. B: Condens. Matter Mater. Phys.* 2005. **72**, No. 4. P. 045423. doi: 10.1103/PhysRevB.72.045423.
40. Barchuk M., Holý V., Miljević B., Krause B., Baumbach T., Hertkorn J. and Scholz F. X-ray diffuse scattering from threading dislocations in epitaxial GaN layers. *J. Appl. Phys.* 2010. **108**, No. 4. P. 043521. doi: 10.1063/1.3460803.

Authors and CV

Oleksii I. Liubchenko, born in 1991, graduated from the National Technical University of Ukraine "Igor Sikorsky Kyiv Polytechnic Institute" in 2015 and postgraduate study at the V. Lashkaryov Institute of Semiconductor Physics. Since 2018, he is the junior researcher at Department for Diffraction Analysis of the Structure of Semiconductors in V. Lashkaryov Institute of Semiconductor Physics, NASU. The area of scientific interests is material analysis sciences, high-resolution X-ray diffraction and computer simulation of XRD spectra. He authored 6 articles.
E-mail: lubchenco.a@gmail.com

Vasyl P. Kladko, Doctor of Sciences (Physics and Mathematics), Corresponding Member of the National Academy of Sciences of Ukraine, Head of the Department of Structural and Elemental Analysis of Materials and Systems at the V. Lashkaryov Institute of Semiconductor Physics, National Academy of Sciences of Ukraine. Author of more than 300 publications. His research interests include: solid-state physics, dynamical theory of diffraction of radiation, X-ray optics, X-ray diffraction analysis of semiconductor crystals, hetero- and nanosystems.

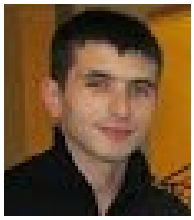

H.V. Stanchu, born in 1987. Work experience: junior researcher at the V. Lashkaryov Institute of Semiconductor Physics, NAS of Ukraine. PhD student at the University of Arkansas. Authored over 18 peer-reviewed articles. The area of his scientific interests includes solid state physics, crystal characterization, and materials science.

Tomash Sabov, born 1992 in Uzhgorod (Ukraine), graduated in electronics 2015 (Kyiv Polytechnic Institute), since 2015 he is a Ph.D. student at the V. Lashkaryov Institute of Semiconductor Physics, NASU. Since 2018 he is a junior researcher at the Department of Ion Beam Engineering at the V. Lashkaryov Institute of Semiconductor Physics. He is author of more than 20 publications. His main research activity is physics of thin films, chromogenic materials and SIMS analysis.

Victor P. Melnik, Doctor of Sciences (Physics and Mathematics), Senior Researcher, Department of Ion-Beam Engineering, V. Lashkaryov Institute of Semiconductor Physics, National Academy of Sciences of Ukraine. Author of more than 150 publications. His research interests include: solid-state physics, ion-beam material synthesis, SIMS spectroscopy.

Serhii B. Kryvyi, born in 1991, defended his PhD thesis in solid state physics in 2017. Researcher at the Department of Structural and Elemental Analysis of Materials and Systems, V. Lashkaryov Institute of Semiconductor Physics, NAS of Ukraine. Postdoctoral fellowship in Laboratory of X-ray and Electron Microscopy Research, Institute of Physics Polish Academy of Sciences. Authored 14 articles and 1 patent. The area of his scientific interests includes solid state physics, real crystal structure, and materials science.

A.E. Belyaev, Director of V. Lashkaryov Institute of Semiconductor Physics, Academician of NAS of Ukraine, Professor, Doctor of Sciences. The area of his scientific interests includes electrical and galvanomagnetic properties of semiconductors.